Volume 14, Issue 3, 142430 (1-13)

Iranian Journal of Catalysis (IJC)

https://doi.org/10.57647/j.ijc.2024.1403.30

Highly efficient hydrogen peroxide decomposition using platinum/palladium alloy nanoparticles anchored on surface-functionalized carbon nanotubes

Akram Dourani, Majid Haghgoo*

Institute of Materials and Energy, Isfahan, Iran.

***Corresponding author:** majid.haghgoo@gmail.com

Original Research

Received:
28 April 2024
Revised:
30 June 2024
Accepted:
10 July 2024
Published online:
20 July 2024

Abstract:

This study reports the development of a novel hybrid catalyst comprising platinum (Pt) and palladium (Pd) nanoparticles encapsulated in multi-walled carbon nanotubes (MWCNT) functionalized with Poly (citric acid) (PCA) and supported on an aluminosilicate substrate. The MWCNTs were covalently grafted with PCA to enhance their catalytic efficiency in hydrogen peroxide (H_2O_2) decomposition. Comprehensive characterization using FESEM, TEM, BET surface area analysis, XRD, XPS, H2-TPR, and reactor decomposition tests revealed superior catalytic performance compared to carboxylated MWCNT counterparts. The MWCNT-g-PCA-Pt/Pd, MWCNT-g-PCA-Pt, and MWCNT-g-PCA-Pd nanocatalysts demonstrated significant improvements in H_2O_2 decomposition efficiency of 100%, 96%, and 89%, respectively. Notably, the PCA-grafted Pt/Pd hybrid alloy nanocatalysts exhibited a 30% increase in specific surface area and a 100% increase in turnover frequency (TOF). These enhancements are attributed to the porous structure of MWCNT-graft-PCA and the optimal distribution of the active catalytic phase on the substrate. The results suggest that this novel catalyst design holds significant promise for applications requiring efficient H_2O_2 decomposition.

Keywords: Carbon nanotubes–grafts-poly (citric acid); Platinum nanoparticles; Catalyst activity, H_2O_2 decomposition

1. Introduction

Green nanotechnology has emerged as a crucial area in technological research and development, offering significant advantages in the production and storage of renewable and clean energy. This field employs nanoscale tools and materials to enhance the efficiency and application of various renewable energy sources, including solar, wind, and hydrogen [1]. In the context of renewable and clean energy production and storage, nanotechnology has the potential to reduce costs, increase efficiency, and mitigate environmental impacts. These advancements contribute to the development of clean and sustainable energy systems, aiding in environmental preservation and reducing dependence on non-renewable energy sources [2, 3].

Hydrogen peroxide (H_2O_2) plays a vital role in green nanotechnology as a powerful oxidizing agent. Its applications in nanotechnology processes include the production of nanoparticles and nanomaterials, offering advantages such as reduced use of polluting and toxic chemicals, increased process efficiency, and minimized generation of hazardous waste. For instance, H_2O_2 is utilized in the synthesis of silver, gold, and conductive oxide nanoparticles [4, 5].

As an environmentally friendly compound that decomposes into oxygen and water, H_2O_2 finds extensive applications in water treatment [6], bleach production [7], fuel cells [8], pharmaceuticals [9], and food industries [10]. However, the slow decay of H_2O_2 under typical conditions, accelerated at higher temperatures, presents challenges in handling and management. Catalysts offer a solution by enhancing and controlling the reaction [11].

Over 100 materials have been identified with catalytic properties for H_2O_2 decomposition [12, 13]. Metal oxides such as Fe_2O_3 [14], MnO_2 [15], and TiO_2 [16] are commonly

used, but their effectiveness may be suboptimal for high-concentration H_2O_2, and many are depleted during the process [17]. Additional drawbacks include rapid deactivation due to metal ion contaminants and the production of undesirable metal phases [18].

Noble metals, including Pt [18], Pd [19], Au [20], and Ag [21], have demonstrated superior performance and are popular catalyst choices. Among these, the Pt-Pd nanocatalyst has garnered particular interest due to its exceptional selective power and ability to withstand various reactions [22, 23].

The catalytic decomposition reaction of H_2O_2 is an exothermic reaction according to Equation. 1 [24]:

$$H_2O_2(l) \longrightarrow H_2O(l) + \frac{1}{2}O_2(g) + 98.11\,\text{kJ/mol} \quad (1)$$

The following model is presented for the decomposition of H_2O_2 on a platinum catalytic surface by Mededovic [25]:

$$H_2 + 2\,Pt \longleftrightarrow 2\,Pt - H \quad (2)$$

$$\frac{1}{2} + Pt \longrightarrow Pt - O \quad (3)$$

$$Pt + OH^- \longleftrightarrow Pt^-(OH)_{ads} + e^- \quad (4)$$

$$Pt - (OH)_{ads} + H_2O_2 \longrightarrow Pt - (OOH)_{ads} + H_2O \quad (5)$$

$$Pt - H + H_2O_2 + e^- \longrightarrow Pt + H_2O + OH^- \quad (6)$$

$$Pt - (OOH)_{ads} + Pt - (OOH)_{ads} \longleftrightarrow 2\,Pt + O_2 + H_2 \quad (7)$$

$$Pt - O + 2\,Pt - H \longleftrightarrow Pt{-}H_2O + 2\,Pt \quad (8)$$

$$Pt - H_2O \longrightarrow Pt + H_2O \quad (9)$$

The initial stages of catalytic hydrogen peroxide decomposition involve the adsorption of molecular hydrogen, oxygen, and hydroxyl ions. Hydrogen and oxygen undergo dissociative adsorption, forming direct bonds with the platinum surface, while hydroxyl ions participate in a straightforward charge transfer reaction. These surface-bound species interact with hydrogen peroxide, producing oxygen and water. Analysis of the species balance reveals that Pt–(OH) and Pt–(H) play direct roles in the decomposition kinetics [19]. The exothermic nature of catalyst-induced hydrogen peroxide decomposition facilitates subsequent spontaneous reactions. The effective catalytic activity requires the even distribution of active metal particles and the prevention of their agglomeration. The addition of ligands [26] and stabilizers [27] to the metal solution has been shown to mitigate clustering.

Carbon nanotubes (CNTs) serve as excellent catalyst supports due to their unique physical properties and ability to optimally support active-phase metal particles. However, their low dispersal in aqueous or organic phases hinders the effective transfer of these properties. Covalent functionalization of nanotube surfaces has been proposed to harness these properties on a larger scale [28, 29].

Despite enhancement with functional groups through oxidation processes, uniform distribution of metal nanoparticles on CNT catalyst supports remains challenging due to their propensity for agglomeration [30, 31]. Covalent functionalization of nanotube surfaces with various groups offers a promising strategy to achieve desirable properties on a macroscopic scale [31].

Formation of functional groups through defect sites on CNT walls and open ends during oxidation with strong acids (e.g., HNO_3 and H_2SO_4) or their mixtures can enhance nanotube reactivity and introduce hydroxyl or carbonyl groups. These groups facilitate chemical reactions such as polymer grafting [32], silanization [33], amination [34], and thiolation [35]. However, the tendency of nanotubes to agglomerate and the spontaneous formation of nanoparticles at surface defect sites continue to pose challenges in achieving uniform distribution of metal nanoparticles on CNT catalyst supports.

Previous research [36] has detailed the development of a novel catalyst using encapsulated platinum particles with water-dispersible MWCNT-g-PCA hybrid material, enhancing nanoparticle dispersion and catalytic activity.

This study presents the first description of a new catalyst with improved distribution and increased catalytic effectiveness for H_2O_2 decomposition. The process involves coating an aluminosilicate granule substrate with MWCNT-g-PCA-Pt/Pd nanoparticles and modifying CNTs with polymers using covalent attachment. Citric acid-based PCA is selected for its cost-effectiveness and availability, enhancing the performance of the resulting catalysts.

2. Experimental section

2.1 Materials

Multi-walled carbon nanotubes (COOH content: 2.6 %, length: 5 μm, outer diameter: 10-15 nm, and number of walls: 3–12) were purchased from Plasma Chem. Monohydrate citric acid, tetrahydrofuran (THF), cyclohexane, sodium borohydride ($NaBH_4$), chloroplatinic acid (H_2PtCl_6,$6H_2O$) and palladium chlorides ($PdCl_2$), hydrogen peroxide solution (50 wt.% in H_2O, stabilized) and aluminosilicate (mesostructured MCM-41 ,$(SiO_2)_{0.9875}(Al_2O_3)_{0.0125}\cdot xH_2O$)were purchased from Sigma-Aldrich.

2.2 Characterization

The morphology of MWCNT-g-PCA-Pt was investigated using scanning electron microscopy (TESCAN MV2300T/40 -TS 5136MM). Fourier transforms infrared (FTIR) spectra were obtained with a spectrometer (Magna-IR 560 Thermo / Nicolet Magna-IR 560). The specific surface area of the samples was measured by N_2 adsorption-desorption isotherms at 77K by the Brunauer–Emmett–Teller (BET) method using a Sorptomatic 1990 apparatus. Thermal gravimetric analysis (TGA) was performed by TGA 2950, TA Instruments from ambient to 1000 °C at a heating rate of 10 °C/min in air atmosphere to evaluate the thermal stability of catalysts. The distribution state of nanoparticles was observed using transmission electron microscopy (TEM, LIBRA 200 MC, Carl Zeiss SMT, Germany, 200 kV). The atomic concentration of the catalyst samples was studied by X-ray photoelectron spectroscopy (XPS, BESTEC GmbH spectrometer) with monochromatized Al K radiation (120W). The X-ray Diffraction pattern of the nanocatalyst was collected on a Philips analytical X-ray diffractometer

(XPertMPD) with monochromatized Cu K_α. The metal phase content of nanocatalysts was measured by the inductively coupled plasma with optical emission spectroscopy (ICP-OES, Vista-MPX, Varian).

The hydrogen temperature-programmed reduction (H_2-TPR, Micrometrics TPD-TPR 2900 analyzer) technique was employed for the evaluation of the reducibility of the nanocatalysts. First, the impurities were removed from the catalyst surface by preheating under a helium atmosphere at 200 °C for 1 h. After cooling the samples, TPR was obtained under 5% H_2 in an argon stream during a linear heating program of 10 to 700 °C at atmospheric pressure, and then H_2 desorbed from the catalyst was monitored by a thermal conductivity detector (TCD).

The catalytic decomposition of hydrogen peroxide was conducted using a custom-designed apparatus. The setup consisted of a sealed stainless steel reactor vessel equipped with three ports: one for gas outlet, one for a safety valve, and one for hydrogen peroxide introduction. The reactor was maintained at a constant temperature of 45 °C using a thermostat with a water circulation system.

The experimental procedure involved initially placing 100 mg of catalyst in the reactor, followed by the injection of approximately 5 ml of H_2O_2. The generated gases were passed through a saturated brine trap to remove H2O and unreacted H_2O_2, with the remaining gas collected for measurement.

The liberated oxygen was directed into an Erlenmeyer flask containing water, which was connected to a second Erlenmeyer flask at atmospheric pressure. Any excess pressure caused water to flow into the second flask, which was positioned on a digital balance with 0.001 g precision to measure the water displaced by oxygen production. This setup allowed for real-time monitoring of H_2O_2 decomposition kinetics.

The decomposition percentage x of H_2O_2 at time x was calculated as below:

$$X_{H_2O_2} = 1 - \frac{n_{xH_2O_2}}{n_{0H_2O_2}} = \frac{n_{xO_2}}{n_{0O_2}} \tag{10}$$

In this relation, n_{xO_2} is the O_2 mole after x time, and n_{0O_2} is the O_2 mole assuming complete conversion of H_2O_2. The conversion of H_2O_2 was determined by calculating the O_2 mole ratio in the rejected water measured by a digital scale to the O_2 mole if hydrogen peroxide was fully decomposed. The number of released O_2 moles was calculated using the ideal gas law, where p represents atmospheric pressure, V is the released O_2 volume, R is the ideal gas constant, and T is the ambient temperature.

Although catalytic decomposition of H_2O_2 is complex, under certain operating conditions in the first 30 seconds, the reaction kinetics can be described by a pseudo-first-order equation:

$$\frac{dn_{\mathrm{H2O2}}}{dt} = -kn_{\mathrm{xH_2O_2}} \tag{11}$$

$$\ln \frac{n_{0\mathrm{H_2O_2}}}{n_{\mathrm{xH_2O_2}}} = kt \tag{12}$$

Turnover frequency (TOF) is the amount of H_2O_2 conversion per amount of catalyst per hour and is calculated as equation. 13:

$$TOF = \frac{dn_{\mathrm{H2O2}}}{dt \times n_{\mathrm{metal}}} = \frac{2n_{\mathrm{x,O_2}}}{t \times n_{\mathrm{metal}}} = \frac{2\frac{pv}{RT}}{t \times n_{\mathrm{metal}}} \tag{13}$$

where n_{metal} is the moles of metal.

2.3 Preparation of MWCNT-COOH- Pt/Pd nanocomposites

complexation and reduction of metal ions in two steps lead to the formation of MWCNT-COOH- Pt/Pd nanocatalysts. Typically, for preparation of MWCNT-COOH-Pt/Pd nanocomposite with the ratio of platinum:palladium ions equal to 2:1, 0.2 g of CNTs-COOH is diluted in 10 ml of water, and then 0.52 g of chloroplatinic((Merck, 40 Pt) acid and 0.26 g of palladium chloride (Merck, 40 Pt) added to it. The mixture was ultrasonicated for 20 minutes and then stirred at room temperature for 3 hours. Then Pt and Pd reduction was conducted by adding 0.05 ml, 0.01 M aqueous sodium borohydride to the mix at room temperature for about one hour. It should be noted that the reduction process must be performed immediately after loading the active metal phase.

2.4 Preparation of MWCNT-graft-PCA- Pt/Pd nanocomposites

MWCNT- graft -PCA hybrid materials were prepared using the following procedure [30]. 0.05 g functionalized carbon nanotubes with 2.5 g monohydrate citric acid are pulverized in a mortar to be mixed. Then, the mixture was replaced into a polymerization ampoule equipped with a vacuum pump and a magnetic stirrer and stirred at 120 °C for half an hour. The reaction was continued for one hour at 120 °C and 1.5 hours at 160 °C. The byproduct produced in this process is water, which must be removed from the system to promote the reaction. Therefore, the water vapor generated by the reaction was removed by a vacuum pump. After the above steps, the residue was dissolved in THF solvent, and then cyclohexane was used as a non-solvent.

A water solution containing MWCNT-graft-PCA (0.2 g in 10 ml) was combined with H2PtCl6 (0.52 g in 3 ml) and subjected to ultrasonication for 15 minutes to ensure efficient dispersion of metal ions within the polymeric shell of the nanocomposite. The resulting mixture was then stirred at room temperature for 3 hours.

Subsequently, a reduction process was performed using 0.01 M sodium borohydride at room temperature for 1 hour to form Pt nanoparticles. The encapsulation of palladium ions followed, wherein the resulting solution was mixed with PdCl6 (0.26 g in 3 ml) and subjected to further reduction using aqueous sodium borohydride under similar conditions. This sequential process yielded a nanocomposite material comprising MWCNT-graft-PCA encapsulating both Pt and Pd nanoparticles.

2.5 Deposition of the catalyst on aluminosilicate

The aluminosilicate granules were immersed in prepared MWCNT-graft-PCA-Pt/Pd solution and stirred at 60 °C for 5h. After complete impregnation, the samples were transferred to the oven and dried at 80 °C for 12 hours in the air. This was followed by calcination in a furnace at 500 °C

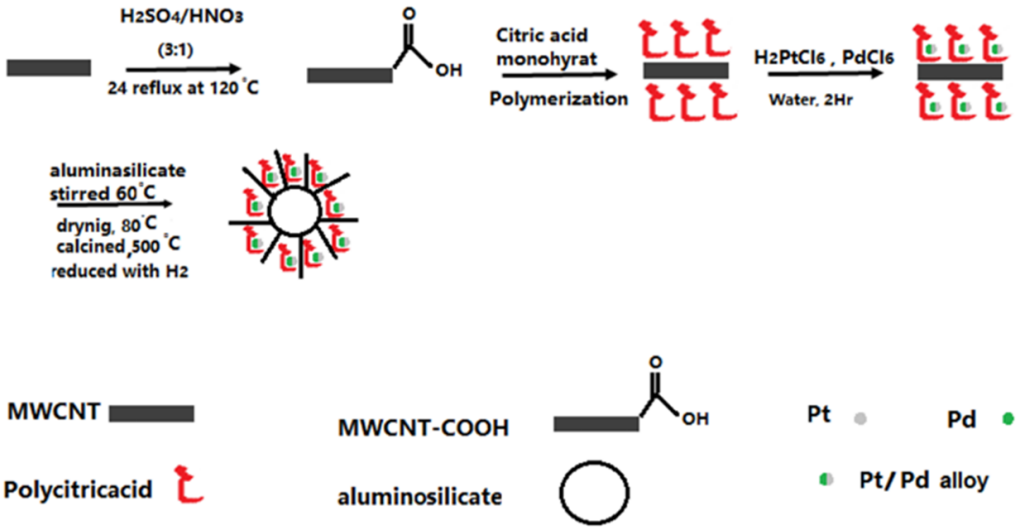

Figure 1. schematic of synthesis steps of MWCNT-g-PCA- Pt/Pd @aluminosilicate.

for 3 hours and reduction operation at 400 °C for 2 hours under a hydrogen atmosphere. The starting weight ratio of the active metal phase to the support in all samples is maintained constant and corresponds to the active metal phase load (related to the mass of the carrier) of 10 wt%.

3. Results and discussion

A schematic of the synthesis method of MWCNT-graft-PCA- Pt/Pd @aluminosilicate is shown in Fig. 1. This figure shows the polycondensation of citric acid on the surface of MWCNT -COOH through covalent bonding between COOH and PCA groups. The figure also illustrates the encapsulation of Pt/Pd nanoparticles by a polymeric shell of MWCNT-g-PCA hybrid materials and aluminosilicate surface coating with a solution of MWCNT-g-PCA-Pt/Pd nanocatalyst. Fig. 2 presents the TEM images of the functionalized MWCNT and the synthesized catalysts. In Fig. 2a, a polymeric shell of the grafted PCA is seen around the nanotubes. According to the microscopic images and regarding the multi-functionality of the opened nanotubes and citric acid, the cross-linking of the nanotubes by citric acid is observed in some parts of the CNT wall during the polycondensation process. The images also show an almost uniform distribution of nanoparticles in the polymeric shell around the sidewall of the nanotubes. The particle size of the metal active phase is almost identical in all samples and has a narrow distribution of 5-10 nm. In fact, the PCA is hyperbranched with its dendritic and void-containing structure. Also, it has negative charge accumulation due to the presence of a large number of oxygen atoms. Therefore, it makes the MWCNT-g-PCA a suitable host for the adsorption of metal ions and proper distribution of particles on the substrate [37, 38]. Fig. 3 shows nanocatalysts' scanning electron microscopy (SEM) images. The results indicated the appropriate dispersion and distribution of metal nanoparticles on all three catalyst samples without any agglomeration. The proper dispersion and uniform distribution of these active agents can play an essential role in enhancing catalytic activity. The EDAX results show that in MWCNT-g-PCA-Pt/Pd nanocomposite, Pt and Pd are distributed in the form of Pt/Pd alloy and not separately.

ICP-AES was used to determine the active metal loading of the catalysts on the support (Table. 1). In all cases, more than 98 wt.% of the materials in the precursors are placed on the support, evidencing the high efficiency of the nanocatalyst synthesis method. Fig. 4a shows typical adsorption-desorption isotherms of the nanocatalysts. All samples show a hybrid of type-II and type-IV isotherms, suggesting the presence of micro-and meso-cylindrical cavities in the nanocatalyst structure. Fig. 4b shows the pore

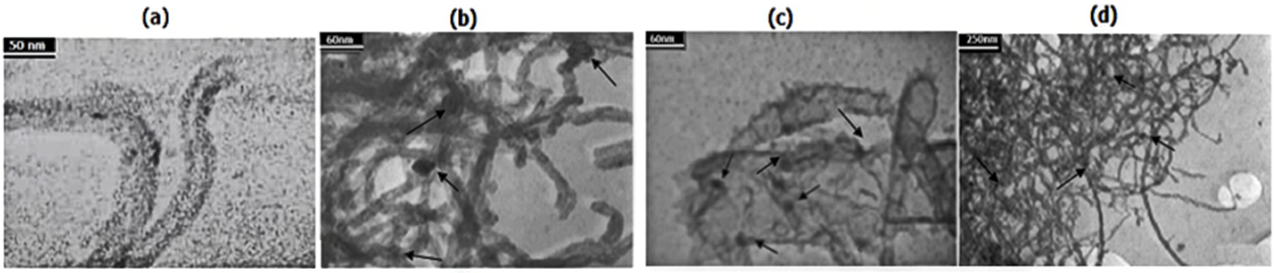

Figure 2. TEM image of (a) MWCNT-g-PCA, (b) MWCNT-g-PCA-Pt, (c) MWCNT-g-PCA-Pd, and (d) MWCNT-g-PCA-Pt/Pd and nanocomposites (black arrows show Pt and Pd nanoparticles).

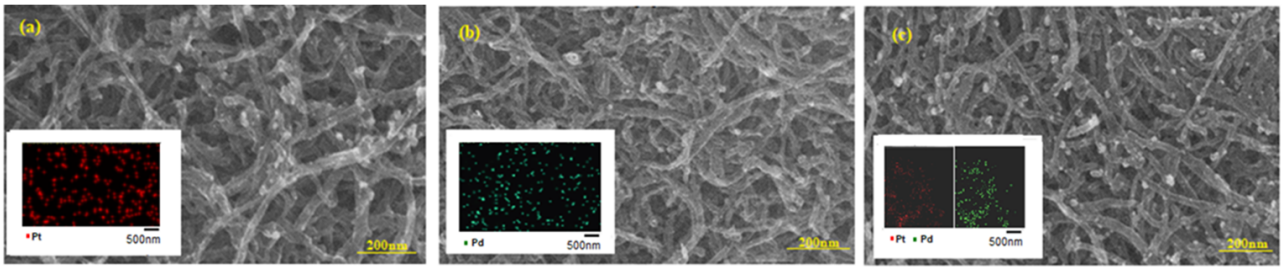

Figure 3. SEM and EDX image of (a) MWCNT-g-PCA-Pt (b) MWCNT-g-PCA-Pd and (c) MWCNT-g-PCA-Pt/Pd @aluminosilicate.

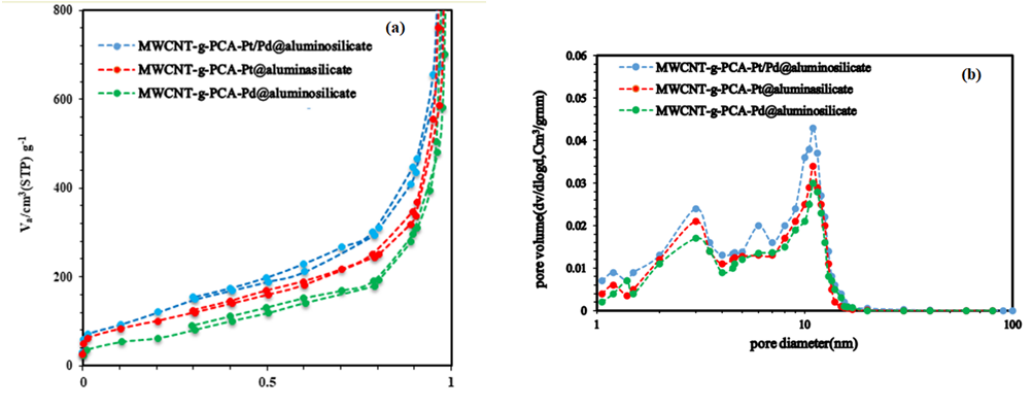

Figure 4. (a) Nitrogen adsorption–desorption isotherms and (b) pore size distribution curves of MWCNT-g-PCA- (Pt, Pd and Pt/Pd) @aluminosilicate nanocatalyst.

size distribution curves of these samples. As can be seen, the pore size distribution of the samples was very narrow in the mesoporous regime, with an average pore size of 10-12 nm. Table. 2 shows the porous characteristics of MWCNT-g-PCA and MWCNT-COOH nanocatalysts on a mesoporous aluminosilicate support. According to the obtained results, the specific surface area of the aluminosilicate pellet is significantly reduced by metal loading on the catalytic substrate [28] due to catalyst deposition on the aluminosilicate surface. Here, D_{ave} of the MWCNT-g-PCA-M@aluminosilicate sample is smaller than that of the aluminosilicate support, indicating the blockage of some pores during the impregnation process [26]. Also, after polymerization with PCA, the S_{BET} of MWCNTCOOH-Pt/Pd@ aluminosilicate nanocatalyst increases from 351 to 460 m^2/g. CNT functionalization with PCA generates repulsion forces, thereby debundling nanotubes and creating more interspace. As a result, it increases the porosity and specific surface area of the nanotubes after polymerization. This process can also facilitate the access of N_2 to the aluminosilicate substrate [38]. The results show that the surface area of the bimetallic sample is slightly higher than that of mono-metallic ones. This difference could be attributed to the increase of the surface roughness [39] by introducing the second metal, which generates more internal defects and creates new micropores [40]. Therefore, the number of catalytic active sites increases and mass transfer is facilitated during the reaction process in bimetallic samples compared to monometallic ones.

The thermal stability of the nanocatalysts was evaluated using TGA analysis (Fig. 5). Carboxylated nanotubes are thermally stable up to 350 °C. A weight loss of 8% at 350 °C can be attributed to the carboxylic groups attached to the CNT surface during functionalization with nitric acid

Table 1. Content of Pt and Pd in precursors and final nanocatalysts ICP-AES analysis.

sample	**Pt wt.% ±0.01**		**Pd wt.% ±0.01**	
	prepared sample	**precursor**	**prepared sample**	**precursor**
MWCNT-g-PCA-Pt@aluminosilicate	9.80	10.00	-	-
MWCNT-g-PCA-Pd@aluminosilicate	-	-	9.70	10.00
MWCNT-g-PCA-Pt/Pd (2:1) @aluminosilicate	6.55	6.65	3.25	3.35
MWCNT-COOH-Pt/Pd (2:1) @aluminosilicate	6.21	6.65	3.15	3.35

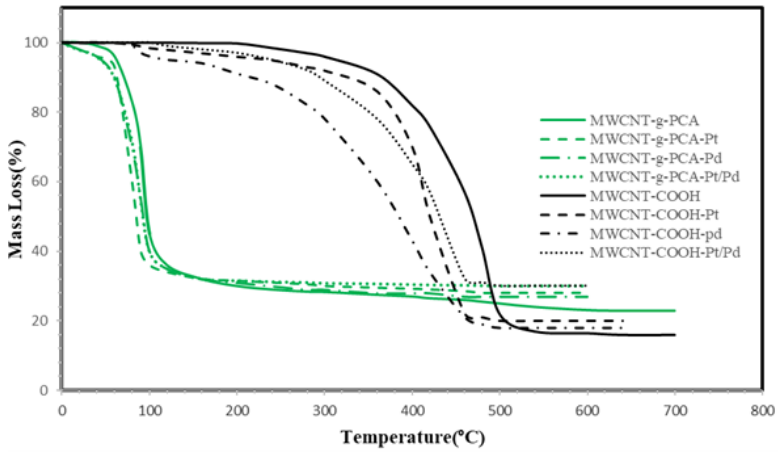

Figure 5. TGA curves of various synthesized @aluminosilicate nanocatalysts.

[41]. Moreover, the weight loss at 400 to 550 °C is due to amorphous carbon oxidation. Compared to carboxylated nanotubes, polymerized nanotubes begin to decompose at a lower temperature. The onset of significant weight loss is 150 °C, at which the nanotube loses 60% of its initial weight due to the decomposition of PCA hyperbranches. The amount of metal phase can be obtained based on the TGA analysis's residual mass, which is in good agreement with the results of the ICP-AES analysis. Although all samples were made with the same values of Pt precursors, the higher values reported from TGA for polymerized samples indicate that the PCA hyperbranch trapped more Pt particles. Also, they had a better anchorage of nanoparticles on the catalyst support.

The XRD patterns of the catalysts are given in Fig. 6. For the carboxylated MWCNT, the peak at the plane (002) observed at 2θ = 25.90 ° corresponds to the diffraction of the nanotubes' graphite structure. The same peak is seen at 2θ = 24.95 ° for polymerized MWCNT. By an increase in the sp^2, carbon-carbon double bond distance can cause a downward shift in the peak (002) for the grafted sample [42]. The other diffraction peaks that appeared at 2θ = 39.65, 46.3, and 67.4 ° are indexed to the (100), (200), and (220) reflections, respectively, for MWCNT-g-PCA-Pt nanocomposite. By adding Pd, the peaks related to Pt^0 are shifted to higher angles. For the Pd (2:1) nanocatalyst, 2θ = 40.30, 47.20,

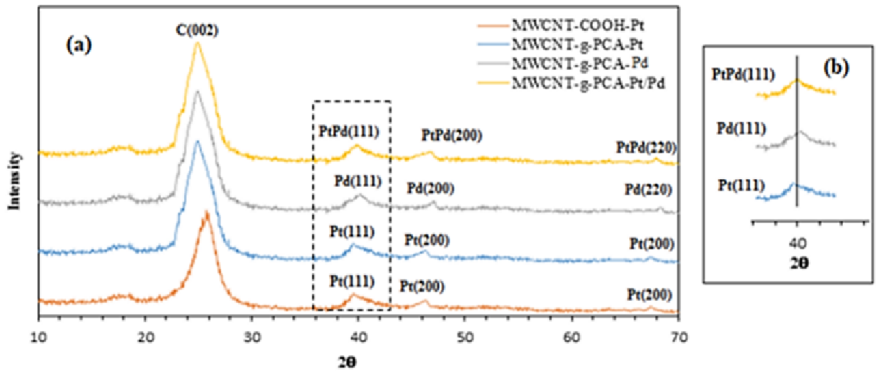

Figure 6. (a) XRD pattern of some nanocatalysts, (b) a magnification of (111) reflection.

Table 2. The porous properties of various nanocatalysts.

Aluminosilicate pellet (Si/Al= 32	920	0.97	12.0	0.83	0.09
MWCNT-g-PCA-Pt@aluminosilicate	442	0.64	11.1	0.42	0.16
MWCNT-g-PCA-Pd@aluminosilicate	438	0.60	10.5	0.38	0.19
MWCNT-g-PCA-Pt/Pd (2:1) @aluminosilicate	460	0.68	11.4	0.53	0.10
MWCNT-COOH-Pt/Pd (2:1) @aluminosilicate	351	0.44	9.6	0.27	0.24

[a] S_{BET} (specific surface area) obtained from Brunauer-Emmett-Teller surface plot
[b] V_{total} (total volume) was obtained from the adsorbed N_2 volume at P/P_0 = 0.99.
[d] Average pore diameter obtained from Barrett-Joyner-Halenda (BJH) plot

and 68.55° are related to the same reflections as those of the Pt nanocatalyst. The XRD peaks for Pt/Pd bimetallic nanocomposite are seen in 2θ = 39.95, 46.25, and 68.10 °, respectively. According to Fig. 6b, the bimetallic catalyst peaks appear between Pt and Pd mono-catalyst. The average lattice parameter obtained for Pt/Pd nanocomposites is consistent with the reports of other researchers. These results confirm the formation of Pd/Pd alloys. This can happen because Pt and Pd have similar atomic sizes and electronic structures, allowing them to form solid solutions (alloys) even in non-equimolar ratios. [43, 44].

As shown in Fig. 7, more detailed information about the composition of the catalyst is obtained using the XPS analysis. Fig. 7(a) shows the XPS spectra of MWCNT-g-PCA-Pt and MWCNT-g-PCA-Pt/Pd nanocatalysts. These spectra confirm the existence of Al 2s (arising from support), C 1s and O 1s (arising from CNT and its surface functional groups), and Pt 4f and Pd 3d (arising from the catalytic active component). Also, Fig. 7(b) presents the Pt 4f core level spectra of the different catalysts. For MWCNT-g-PCA-Pt, two main peaks are observed at binding energy 71.25 eV and 74.43 eV, which are related to the spin-orbital splitting of Pt $4f_{7/2}$ and Pt $4f_{5/2}$ regions, respectively. The peak 4f of MWCNT-g-PCA-Pt/Pd nanocatalyst is positively shifted by about 0.45 eV and 0.54eV compared to that of MWCNT-g-PCA-Pt nanocomposite. This shift is due to the interaction between Pt and Pd and the modification of their electronic structure. Here, the higher binding energies of polymerized nanocatalysts emphasize the strong interfacial interaction between Pt and PCA branches in this case. The high-resolution spectra of C ls for carboxylated and polymerized MWCNT nanocatalysts are shown in Fig. 7(c). Both samples show a major peak at approximately 284.5 eV that corresponds to the graphene-shaped structure of CNT with sp^2 hybridized (C=C). The samples also show a peak at 285.2 eV related to SP^3 hybridizes carbon atoms (C-C). The other peaks at 286.7 eV, 288.1 eV, 289.6 eV, and 291.1 eV are related to carbon atoms attached to one or more oxygen atoms that induce a positive charge on the carbon atoms and are indexed to C-O, C=O, O-C=O, and $\pi - \pi^*$ transitions, respectively [45–47]. Table. 3 compares the atomic concentration data of each component for MWCNT-COOH and MWCNT-g-PCA. A decrease in the sp^2 peak and an increase in the sp^3 peak indicate that the PCA shell caused more breakage of nanotube graphite exterior walls than carboxyl groups. At the same time, oxygenated functional groups increased, indicating that carboxyl groups are covalently attached to MWCNT-COOH.

Fig. 8 shows the TPR spectra of the prepared catalysts. The H_2-TPR profile of the Pt nanocatalysts shows two peaks: the first hydrogen consumption peak is related to the reduction of PtO_2 to metallic Pt, and the second to the reduction of metal Pt-Al to metallic Pt. For MWCNT-COOH-Pt aluminosilicate nanocatalyst, these peaks are observed at 389 and

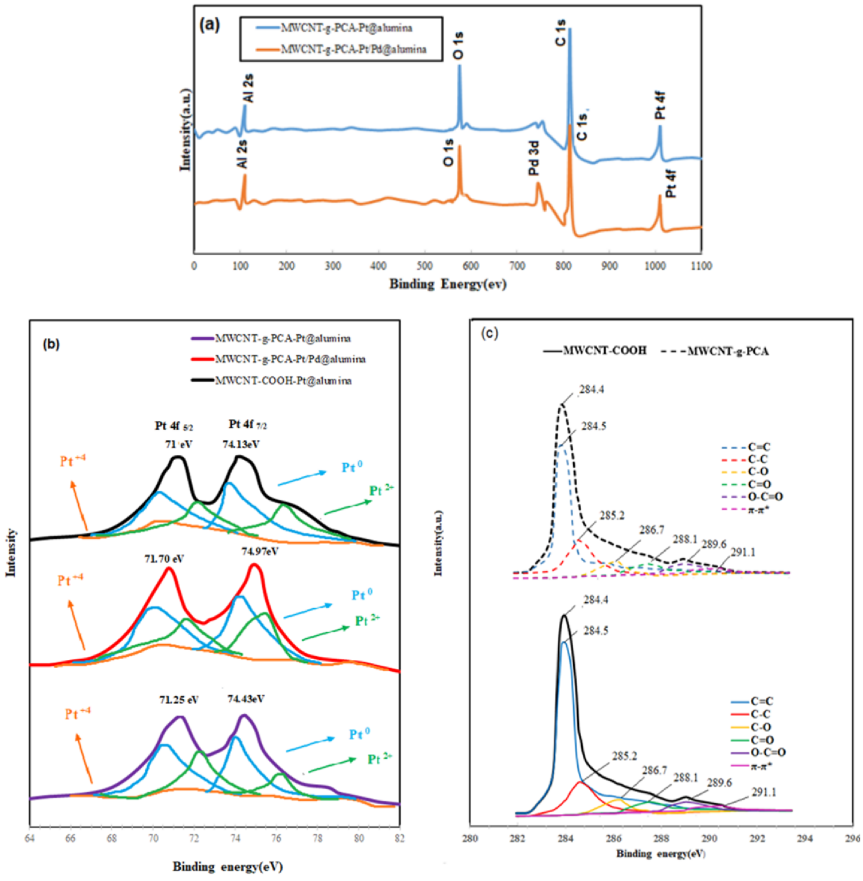

Figure 7. XPS spectra of (a) MWCNT-g-PCA -M (Pt, Pt/Pd) @aluminosilicate nanocatalyst, Pt4f (b) different nanocatalysts, (c)peak fitting results from C 1s of carboxylated and polymerizd MWCNT nanocatalyst.

Table 3. Atomic concentration of carboxylated and polymerized CNT by C1s XPS data.

MWCNT-COOH	60.7	19.2	5.6	4.1	5.8	4.6
MWCNT-g-PCA	53.9	26.3	7.1	2.8	8.2	1.7

598 °C, respectively. Compared to the MWCNT-COOH-Pt nanocatalyst, the reduction temperature of the MWCNT-g-PCA-Pt sample decreased by 25 °C, indicating the enhanced surface activity of the nanoparticles with a uniform distribution in the polymeric shell [43]. Notably, the reduction peak in the sample consisting of encapsulated platinum in polymerized CNT is quite narrow and symmetrical. However, the wide and asymmetrical peak at higher temperatures in the sample containing carboxylated CNT indicated different types of PtO_2 domains with different interactions with support. These domains can be created by the aggregation of PtO_2 clusters, leading to a reduction in surface active areas [48]. For the Pd nanocatalyst, the first peak at 40 °C is related to PdO large crystals, and the negative peak at 100 °C is attributed to the hydrogen evolution of Pd hydrate phase decomposition. The stable peak observed at 240 °C is related to the reduction of PdO nanoparticles with strong interaction with the support [38].

Analysis of the TPR profile of the bimetallic Pd-Pt catalysts reveals behavior distinct from a simple aggregation of monometallic samples. The proximity of Pd and Pt particles is evidenced by the shift in the peak associated with Pd hydrate phase formation. Both the dispersion of Pd particles and the Pt content in the Pd-Pt alloy influence the reduction of the Pd hydrate phase formation.

In the bimetallic catalyst, a negative peak observed at 60 °C corresponds to the palladium hydrate phase. These findings align with those reported by Víctor Santes [49], who noted that the interaction between platinum and palladium modifies the formation temperature of the hydrate phase. The absence of a peak related to PtO reduction on the substrate in bimetallic catalysts suggests the presence of platinum in its metallic form.

MWCNT-g-PCA-Pt/Pd exhibits the highest H_2 consumption during reduction steps, as indicated by the largest surface area under its curve. This corresponds to a greater number of active sites.

FESEM images of used catalysts were obtained to examine surface characteristics, nanoparticle durability, distribution, and potential agglomeration resulting from the catalytic decomposition of hydrogen peroxide (Fig. 9). The images do not show surface denuding typically associated with complete washing. EDAX results indicate an absence of catalyst poisoning, suggesting that the catalyst maintains its efficiency and usability at levels comparable to those before the decomposition test.

Fig. 10 shows H_2O_2 conversion over time in the presence of various catalysts. The reaction rate is also obtained using the slope of this curve. According to the obtained results, the catalytic activity of Pt nanocatalysts in the presence of polymerized carbon nanotubes is higher than that of carboxylated carbon nanotubes. The highest catalytic activity related to MWCNT-g-PCA-Pt/Pd nanocatalyst, which shows an approximately twice increase compared to that of similar bimetallic catalysts without a polymerization pro-

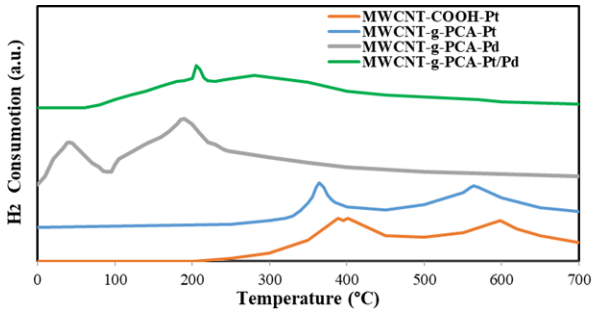

Figure 8. H_2-TPR profile of various nanocatalysts.

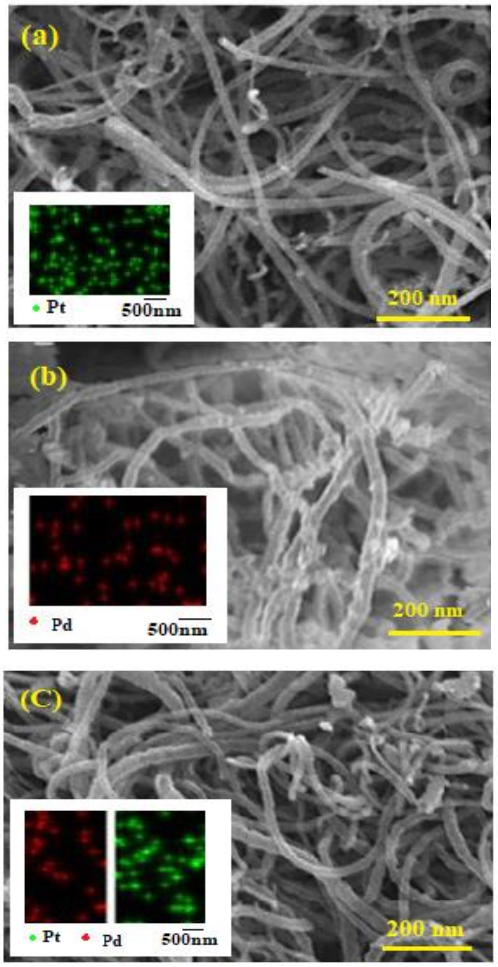

Figure 9. SEM and EDX image of (a) MWCNT-g-PCA-Pt (b) MWCNT-g-PCA-Pd and (c) MWCNT-g-PCA-Pt/Pd @aluminosilicate after catalyst decomposition.

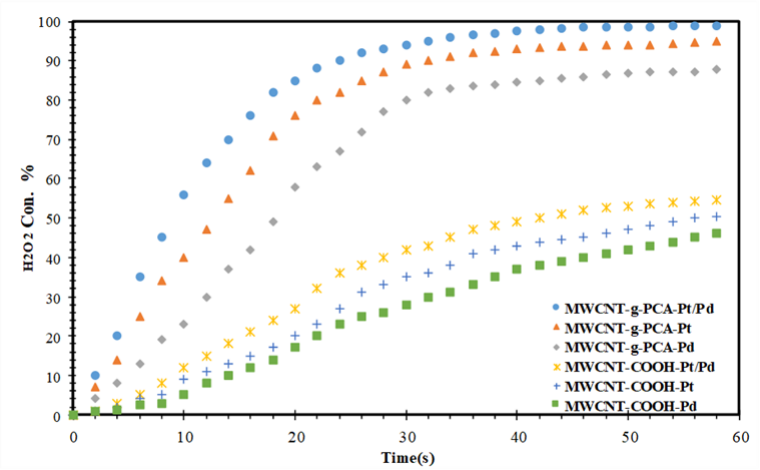

Figure 10. H_2O_2 conversion over time in the presence of various catalysts.

cess and near-complete decomposition occurs after 40 s for the bimetallic polymer catalyst. This result could be due to the better dispersion of Pt on the support surface and the proper interaction of metallic nanoparticles with aluminasilicate in the presence of citric acid polymer chains. These results agree with BET analysis in evaluating the surface properties of various types of synthesized nanocatalysts. Overall, the significant improvement of SBET and surface-active sites in pol polymerized samples compared to carboxylated samples will improve catalytic properties.

Table. 4 summarizes the effects of various parameters on hydrogen peroxide decomposition. The reaction rate constant is expressed by equation. 12. Results indicate that H_2O_2 decomposition follows bimolecular first-order kinetics, consistent with findings from other researchers [24]. At elevated temperatures, H_2O_2 tends toward auto-decomposition, and the low solubility of oxygen at high temperatures shifts the reaction equilibrium forward, resulting in increased reaction rates. However, due to the 50% H_2O_2 concentration used, temperature increases could lead to heat generation, ignition, and potential explosion. Consequently, the temperature parameter's effect on H_2O_2 decomposition was not investigated.

During H_2O_2 decomposition, localized pressure and temperature increases subject the catalyst support to thermal and mechanical stress, potentially causing destruction and

Table 4. Effects of important experimental variables on the catalytical decomposition of H_2O_2.

Parameter	PCA	Value	k (min^{-1}) ±0.01	TOF(min^{-1}) ±1
Pt/Pd	**PCA**			
	✓	**0**	**41.20**	**712**
	✓	**1**	**39.18**	**612**
	✓	**2**	**54.80**	**803**
	✓	**∞**	**56.32**	**830**
		0	**15.91**	**314**
	×	**1**	**17.72**	**370**
	×	**2**	**18.83**	**396**
	×	**∞**	**12.84**	**246**
	×			
Initial pH				
		(Pt=0)		
	✓	**3**	**40.50**	**680**
	✓	**5**	**41.20**	**712**
	✓	**7**	**39.10**	**632**
	✓	**9**	**38.33**	**610**
		(Pd=0)		
	✓	**3**	**33.43**	**580**
	✓	**5**	**48.11**	**760**
	✓	**7**	**56.32**	**830**
	✓	**9**	**54.54**	**801**

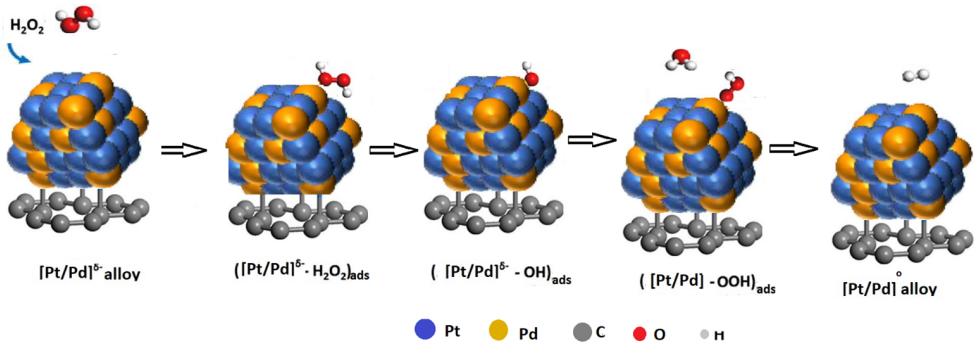

Figure 11. Schematic of hydrogen peroxide decomposition on the prepared catalyst.

sintering. Therefore, a catalytic support with high mechanical and chemical resistance and suitable surface area is essential. The selected alumina-silica supports, chosen for their desired properties, form a constant base across all samples. The porous ceramic catalyst supports used have low thermal conductivity, which can lead to hot spots in the catalyst bed. Carbon nanotubes were incorporated in all samples to enhance thermal conductivity and mitigate this phenomenon, as well as to improve particle distribution.

The metal catalyst's oxidation state is crucial for H_2O_2 decomposition, and catalyst activity requires adjustment in the presence of protons and/or anions in feed solutions [50–53]. The effect of pH on H_2O_2 decomposition activity was evaluated in the range of 3 to 9. The initial pH of the H_2O_2 solution was 5.5, with acidic or basic conditions created by adding 0.1 M H_2SO_4 or 0.1 M NaOH, respectively. Findings indicate that decreasing solution pH slowed the reaction, with this effect more pronounced for the Pd active phase compared to Pt. Oxidized Pd surfaces show greater responsiveness to proton and/or anion interaction, restricting H_2O_2 molecule access and inhibiting decomposition.

Results suggest that platinum and palladium particles in combination carry negative and positive charges, respectively. The presence of more negatively charged particles in the Pt/Pd=2 sample creates an additional negatively charged surface, enhancing catalytic activity by accelerating reactions 4 to 6. Optimal decomposition rates were achieved at an initial pH of 7.5 for the prepared catalysts. The decomposition reaction mechanism according to the obtained data and the Mededovic model [25] is shown in Figure. 11, which includes hydrogen peroxide adsorption on the catalytic substrate and electron transfer from the metal alloy to the adsorbate and a series of intermediate reactions on the metal surface as described above. These absorbed species and intermediate products react with hydrogen peroxide and produce oxygen and water.

To assess catalyst stability and reusability, the prepared catalyst was washed with excess deionized water after each cycle, then dried for 2 hours at 120 °C. The dried catalyst was subsequently used for H_2O_2 decomposition in three consecutive cycles.

Table. 5 presents the reaction rate constant (k) and turnover frequency (TOF) in three cyclic steps in H_2O_2 decomposition. According to the obtained results, in MWCNT-g-PCA-Pt@ aluminosilicate nanocatalyst, the H_2O_2 conversation percentage has decreased from 89 to 78 from the first cycle to the third one. However, in MWCNT-COOH-Pt @ aluminosilicate, this value has decreased from 35 to 21% under the same conditions.

In fact, PCA chains lead to a better distribution of active metal sites and stronger interaction between the metal active phase and support. But in bimetallic nanocatalysts, the cyclic conversion rate has decreased from 94 to 88% for MWCNT-g-PCA-Pt/Pd @ aluminosilicate and from 42 to 31% for MWCNT-COOH-Pt/Pd @ aluminosilicate. In these nanocatalysts, the presence of the second metal in-

Table 5. Comparison of previous reports of HO_2 decomposition rates with the present research work.

Catalyst type	Temperature (k)	TOF (min^{-1})	Reference
MnO_2	298	135	[12]
NaI	298	72	[12]
Ru pincer complex	298	540	[53]
1% AuPd/C	275	167	[54]
Co/Zn-ZIF-8	298	47	[55]
Au/SRAC	303	29	[56]
MWCNT-g-PCA-Pt/Pd@ aluminasilicate	298	830	present work
MWCNT-g-PCA-Pt@aluminasilicate	298	712	present work
MWCNT-g-PCA-Pd@ aluminasilicate	298	616	present work

creases the specific surface area and modifies the electronic structure of Pt nanoparticles. Generally, it is inferred that the catalytic activity is a function of electronics and geometry.

In this work, the catalytic reaction rate for MWCNT-g-PCA-Pt/Pd @ aluminosilicate nanocatalyst for H_2O_2 decomposition is about 830 min^{-1}, which is significant compared to that in similar works. In addition, the durability of the performance of this catalyst is shown in successive cycles. Table. 5 summarizes the catalytic activity of some catalysts for H_2O_2 decomposition in different research works and the present study. According to this table, MWCNT-g-PCA-Pt/Pd@ aluminosilicate has the highest catalytic activity among the reported catalysts.

4. Conclusion

In conclusion, we have developed novel nanocatalysts comprising encapsulated platinum group metal nanoparticles supported on aluminosilicate, utilizing a newly synthesized water-soluble MWCNT-g-PCA hybrid material for H_2O_2 decomposition. The physicochemical properties of these new nanocatalysts were examined and compared with those of Pt@aluminosilicate nanocatalysts developed using carboxylated MWCNT. In polymer-grafted nanotubes, PCA hyperbranching resulted in efficient dispersal of metal nanoparticles on the substrate, while carboxylated nanocomposites exhibited some agglomerated nanoparticles anchored to the nanotube via hydroxyl and carbonyl clusters.

Significantly, the surface area of PCA-bonded CNT catalysts increased by 30% compared to carboxylated CNT, attributed to nanotube segregation and the creation of additional internal voids. The design material featuring a hyperbranched polymer structure as the active phase's base demonstrated an interconnected porous pattern on the supporting surface, substantially enhancing H_2O_2 decomposition rates and catalyst longevity.

MWCNT-g-PCA-Pt/Pd@aluminosilicate exhibited the highest catalytic activity, showing marked improvement over analogous metallic catalysts. In contrast, the catalytic performance of MWCNT-COOH-Pt/Pd@aluminosilicate was less than half that of the polymerized catalyst. The polymerized sample demonstrated exceptional durability through multiple experimental cycles. To our knowledge, this level of catalytic activity for H_2O_2 decomposition is unprecedented in the literature.

Authors Contributions
Authors were equally contributed in acquisition and analysing the data as well as preparing the paper.

Availability of Data and Materials
Data is available on request from the corresponding author, upon reasonable request.

Conflict of Interests
The authors declare that they have no known competing financial interests or personal relationships that could have appeared to influence the work reported in this paper.

References

[1] S. Zinatloo-Ajabshir and M. Salavati-Niasari. *Compos. B Eng.*, **14**(2019):106930. DOI: https://doi.org/10.1016/j.compositesb.2019.106930.

[2] S. Zinatloo-Ajabshir, S. Rakhshani, Z. Mehrabadi, M. Farsadrooh, M. Feizi-Dehnayebi, S. Rakhshani, M. Dušek, V. Eigner, and S. T. M. Aminabhavi. *J.Environmental Management*, **350**(2024):119545. DOI: https://doi.org/10.1016/j.jenvman.2023.119545.

[3] A. Sobhani. *Arab. J. Chem.*, **16**(2023):105201. DOI: https://doi.org/10.1016/j.arabjc.2023.105201.

[4] S. K. Blourfrosh and K. Mahanpoor. *Iran. J. Catal.*, **11**(2021):149–163.

[5] S. Rayatia, M. Etefagha, and M. Masteri-Farahani. *Iran. J. Catal.*, **13**(2023):177–185.

[6] I. Sánchez-Montes, G. O. S. Santos, T. O. Silva, R. Colombo, and M. R. V. Lanza. *J. Clean. Prod.*, **392**(2023):136242. DOI: https://doi.org/10.1016/j.jclepro.2023.136242.

[7] R. F. Tavcer, K. Brencic, R. Fink, and R. B. Tomsic. *Molecules*, **27**(2022):195–201. DOI: https://doi.org/10.3390/molecules27010195.

[8] S. Jeon, H. An, and H. Y. Chung. *Sustain Energy Fuels*, **6**(2022):841–85150. DOI: https://doi.org/10.1039/D1SE01784E.

[9] Y. Zhang, J. Guo, B. Li, Z. Wang, and X. Zunzhu. *J. Water Process Eng*, **56**(2023):104257, . DOI: https://doi.org/10.1016/j.jwpe.2023.104257.

[10] A. M. Abdelshafy, H. Neetoo, and F. Al-Asmari. *J. f Food Protection*, **87**(2024):100306. DOI: https://doi.org/10.1016/j.jfp.2024.100306.

[11] M. Shang, T. Noet, Y. Su, and V. Hosse. *AIChE J.*, **63**(2017):689–698. DOI: https://doi.org/10.1002/aic.15385.

[12] M. S. H. Chowdhury, M. Ahsan, M. H. Kabir, S. S. Alam, and M. Hasnat. *Asian J Chem.*, **34**(2022):1263–1268. DOI: https://doi.org/10.14233/ajchem.2022.23729.

[13] P. Pedziwiatr, F. Mikolajczyk, D. Zawadzki, K. Mikolajczyk, and A. Bedka. *Acta Innovations*, **26**(2018):45–52. DOI: https://doi.org/10.32933/ActaInnovations.26.5.

[14] M. H. Vafaei, W. Geng, Y. Wei, J. Miao, S. Yu, A. Shahi, C. Chen, and M. Long. *Chemo .sphere.*, **291**(2022):133037. DOI: https://doi.org/10.1016/j.chemosphere.2021.133037.

[15] J. H. Gartlein, D. M. Morales, A. Raba, T. Bredow, W. Schuhmann, and M. Behrens. *Chem. Eu .J.*, **26**(2020):12256 – 12267. DOI: https://doi.org/10.1002/chem.201905090.

[16] D. Santhanaraj, A. Selvamani, K. Rajakumar, J. N. Ricky, and S. Giridhar T. *New.J. Chem*, **45**(2021):9944–9958. DOI: https://doi.org/10.1039/D1NJ00499A.

[17] J. Y. Lestrade, P. Prévot, J. Messineo, and S. Anthoine. *Space Propulsion Conference*, (2016).

[18] K. Heck, K. Y. Wang, G. Wu, and F. Wang. *RSC. Adv.*, **9**(2019):27042–27049. DOI: https://doi.org/hal-01353568.

[19] R. Serra-maia, M. Bellier, S. Chastka, K. Tranhu, A. Subowo, J. D. Rimstidt, P. M. Usov, A. J. Morris, and F. M. Michel. *ACS Appl Mater Interfaces*, **10**(2018):21234–21224. DOI: https://doi.org/10.1021/acsami.8b02345.

[20] S. M. Taghavi Kouzehkanan, J. E. Hong, and T. S. Og. *J.Materials science.*, **58**(2023):5178–5185. DOI: https://doi.org/10.1007/s10853-023-08346-1.

[21] K. Liu, S. He, S. L. Li, Y. Liu, Z. Huang, T. Liu, H. Wu, X. Jiang, and K. Liu. *Sci Rep.*, **11**(2021):9709. DOI: https://doi.org/10.1038/s41598-021-89235-y.

[22] Z. Ki, L. Klintberg, K. Palmer, and G. Thorne. hydrogen peroxide monopropellant ceramic microthruster. *J. Propuls. Power.*, **9**(2020)(3):216. DOI: https://doi.org/10.1016/j.jppr.2020.08.00.

[23] M. M. Alam, M. H. Kabir, M. Ahsan, S. M. B. Uddin, I. A. Siddiquey, and M. A. Hasnat. *Am.J .Chem.*, **9**(2019):115–122. DOI: https://doi.org/10.5923/j.chemistry.20190904.02.

[24] M. A. Hasnat, M. M. Rahman, S. M. Borhanuddin, A. Siddiqua, N. M. Bahadu, and M. R. Karim. *Catal. Commun.*, **12**(2010):286–291. DOI: https://doi.org/10.1016/j.catcom.2010.10.001.

[25] S. Mededovic´ and B. R. Locke. *Appl. Catal., B*, **67**(2006):149–159. DOI: https://doi.org/10.1016/j.apcatb.2006.05.001.

[26] Z. Amirsardari, A. Dourani, M. A. Amirifar, N. Gadiri Massoom, and A. H. Javadi. *Chem .Pap.*, **74**(2020): 3233–3241, . DOI: https://doi.org/10.1007/s11696-020-01148-8.

[27] M. Farsadrooh, M. Noroozifar, A. R. Modarresi-Alam, and H. Saravani. *Compos B Eng*, **160**(2019):505–511. DOI: https://doi.org/10.1016/j.compositesb.2018.12.008.

[28] Z. Amirsardari, A. Dourani, M. A. Amirifar, and N. Gadiri Massoom. *Mater .Chem .Phys.*, **239**(2020):122015, . DOI: https://doi.org/10.1016/j.matchemphys.2019.122015.

[29] P. R. Kotha, M. Attari, M. Maschmann, and F. Bunyak. *IEEE Applied Imagery Pattern Recognition Workshop*, (2023).

[30] M. Dourani, A. H. Haghgoo, and M. Hamadanian. *Compos. B Eng.*, **176**(2019):107299. DOI: https://doi.org/10.1016/j.compositesb.2019.107299.

[31] H. Shahbazi, A. Shafei, and S. Sheibani. *AIP Conference Proceeding*, (2018).

[32] B. V. Basheer, J. J. George, S. Siengchin, and J. Parames. *Nano-Struct*, **22**(2019):100429. DOI: https://doi.org/10.1016/j.nanoso.2020.100429.

[33] M. T. Kim, K. Y. Rhee, S. J. Park, and D. Hui. *Compos B. Eng.*, **43**(2012):2298–2302. DOI: https://doi.org/10.1016/j.compositesb.2011.12.007.

[34] A. Andrés Nistal, B. G. Falzon, S. C. Hawkins, R. Chitwan, C. García-Diego, and F. L. Rubio. *Compos B. Eng.*, **165**(2019):537–544. DOI: https://doi.org/10.1016/j.compositesb.2019.107711.

[35] H. Azizi, H. Fallahi, I. Ghasemi, M. Karrabi, and M. Nazemian. *J. Vinyl. Addit. Technol.*, **26**(2020):113–126. DOI: https://doi.org/10.1016/j.compositesb.2019.02.001.

[36] N. Sarlak, M. Karimi, and A. Dourani. *J. Nanosci. Nanotechnol.*, **14**(2014):6907–69014. DOI: https://doi.org/10.1166/jnn.2014.8961.

[37] A. Bahari, H. Hekmatara, R. Sepahvand, and M. Adeli. *Nano*, **3**(2008):37–44. DOI: https://doi.org/10.1142/S1793292008000824.

[38] M. Adeli, B. Rasoulian, F. Saadatmehr, and F. Zabihi. *J. App.l Polym .Sci.*, **129**(2013). DOI: https://doi.org/10.1002/app.39028.

[39] S. Bhogeswararao and D. Srinivas. *J. Catal.*, **327**(2015):65–77. DOI: https://doi.org/10.1016/j.jcat.2015.04.018.

[40] W. S. Abo El-Yazeed and A. I. Ahmed. *RSC Adv.*, **9**(2019):18803–18813. DOI: https://doi.org/10.1039/C9RA03310F.

[41] B. Lu, Q. Liu, F. Nichols, R. Mercado, D. Morris, N. Li, P. Zhang, P. Gao, Y. Ping, and S. Chen. *Research*, (2020):1–12. DOI: https://doi.org/10.34133/2020/9167829.

[42] M. Dehghani-dashtabi, H. Hekmatara, and J. Seyedyazdi. *Chem. Phys.*, **224**(2019):271–278. DOI: https://doi.org/10.1016/j.matchemphys.2018.12.032.

[43] B. Gindana, A. A. Jamil, B. Brandon, B. Jr, F. Tan, J. A. Asik, and R. Idris. *Adv. Mater. Res.*, **1107**(2015):320–325. DOI: https://doi.org/10.4028/www.scientific.net/AMR.1107.320.

[44] H. Chen, Y. Liang, T. Chen, Y. Tseng, C. Liu, S. Chung, C. Hsieh, C. Lee, and K. Wang. *Chem. Comm.*, **76**(2014):11165–11168. DOI: https://doi.org/10.1039/C4CC04595E.

[45] S. Ghosh, R. K. Sahu, and C. R. Raj. *Nanotechnology*, **23**(2012):385602. DOI: https://doi.org/10.1088/0957-4484/23/38/385602.

[46] I. A. Chetyrin, C. Mendeleev, A. V. Bukhtiyarov, I. P. Prosvirin, and V. I. Bukhtiyarov. *IMendeleev Commun.*, **31**(2021):635–637. DOI: https://doi.org/0.1088/0957-4484/23/38/385602.

[47] J. Oenema, J. P. Hofmann, E. J. Hensen, J. Zečević, and K. P. Jong. *Chem.Chat.Chem.*, **12**(2020):615–622. DOI: https://doi.org/10.1002/cctc.201901617.

[48] Z. Zhang, L. Pfefferle, and G. L. Haller. *Chinese. J. Catal.*, **35**(2014):856–863, . DOI: https://doi.org/10.1002/cctc.201901617.

[49] R. M. Guerrero, A. Hernández-gordillo, V. Santes, J. Roberto, V. García, J. Escobar, L. Díaz-garcía, L. Díaz, B. Arceo, and V. G. Febles. *J. Chem.*, **1**(2014):1–10. DOI: https://doi.org/10.1155/2014/679281.

[50] T. Tamiji and A. Nezamzadeh-Ejhieh. *J. Taiwan Inst. Chem. Eng.*, **04**(2019):130–138. DOI: https://doi.org/10.1016/j.jtice.2019.08.021.

[51] N. Raeisi Kheirabadi, A. Nezamzadeh Ejhieh, and H. Aghaei. *Iran. J. Catal.*, **11**(2021)(2):181–189.

[52] M. Rezaei and A. Nezamzadeh-Ejhieha. *Int. J. Hydrogen Energy*, **45**(2020):24749. DOI: https://doi.org/10.1016/j.ijhydene.2020.06.258.

[53] M. Nielsen. *ChemLett.*, **14**(2016):359–365. DOI: https://doi.org/0.1007/s10311-016-0576-0.